

## Supporting information

### Eco-Friendly Lead-Free Halide Double Perovskites $A_2CuMCl_6$ (A=K, Rb; M=Sb, Bi): Stability, Thermoelectric, and Optoelectronic Advancements Through Theoretical Insights

Mudasir Younis Sofi<sup>1</sup>, Mohd Shahid Khan<sup>1</sup>, M. Ajmal Khan<sup>\*,1</sup>

<sup>\*,1</sup>Department of Physics, Jamia Millia Islamia, New Delhi-110025

**\*Email: majkhan@jmi.ac.in**

#### I. Goldschmidt tolerance factor ( $t$ ), octahedral factor ( $\mu$ ) and new tolerance factor ( $\tau$ ) of $A_2CuMCl_6$ (A = K, Rb, M= Sb, Bi) double halide perovskites.

Goldschmidt tolerance factor ( $t$ ) and octahedral factor ( $\mu$ ) are given as:

$$t_{dp} = \frac{r_A + r_X}{\sqrt{2}r_{BB'} + r_X}, \mu = r_B/r_X$$
 where  $r_A$ ,  $r_B$ , and  $r_X$  are the Shannon ionic radii for  $A^+$ ,  $B^+$ ,  $B'$  and  $X^-$  ions, respectively.

For stable cubic perovskites, the ranges of  $t$  and  $\mu$  are  $0.8 \leq t_{dp} \leq 1.0$  and  $0.29 \leq \mu \leq 0.55$ . The calculated values in Table S1 show that the considered perovskites are stable in cubic structures at room temperatures.

Recently, Bartel et al. have reported a new tolerance factor ( $\tau$ ) to predict the stability of a

perovskite, which is given as:  $\tau = \frac{r_X}{r_B} - n_A \left( n_A - \frac{r_A/r_B}{\ln(r_A/r_B)} \right)$ , where  $n_A$  is the oxidation state of A,  $r_i$  is the ionic radius of ion  $i$ ,  $r_A > r_B$  by definition, and  $\tau \ll 4.18$  indicates perovskite (92% accuracy).

**Table S1: Intended values of the tolerance factor  $t_{dp}$ , octahedral factor  $\mu$  and new tolerance coefficient  $\tau$  of  $A_2CuMCl_6$  perovskites**

Material	$t_{dp}$	$\mu$	$\tau$
$K_2CuSbCl_6$	0.95	0.43	4.16
$Rb_2CuSbCl_6$	0.97	0.43	4.14
$K_2CuBiCl_6$	0.91	0.50	4.04
$Rb_2CuBiCl_6$	0.93	0.50	3.97

#### II. DFT simulated XRD patterns of $A_2CuMCl_6$ double halide perovskites.

Density Functional Theory (DFT) simulations have been utilized to generate X-ray Diffraction (XRD) patterns for the specified materials. These simulated plots exhibit a satisfactory level of concurrence with experimental findings from analogous materials such as  $\text{Cs}_2\text{CuSbCl}_6$  and  $\text{Cs}_2\text{AgBiCl}_6$ . [1-2].

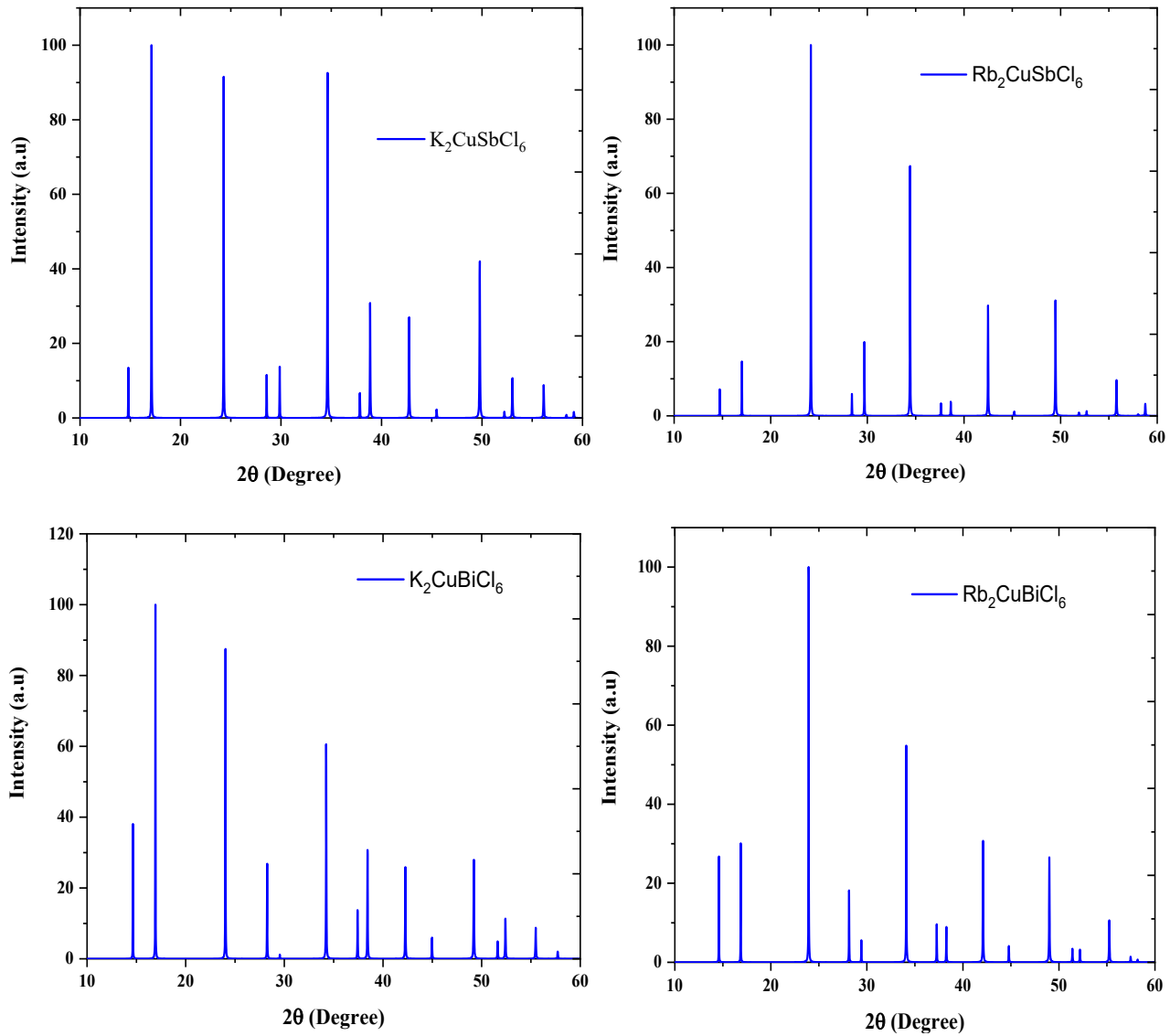
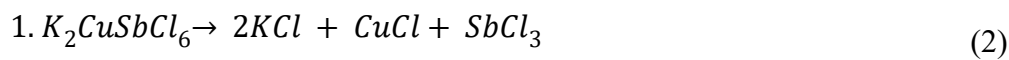


**Figure S1.** The DFT simulated XRD patterns of  $\text{A}_2\text{CuMCl}_6$  double halide perovskites.

### III. Thermodynamic stability

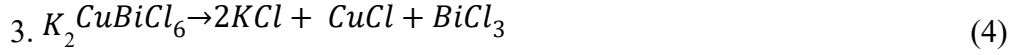
Reactions for decomposition of  $\text{A}_2\text{CuMCl}_6$  double halide perovskites has been estimated as follows:



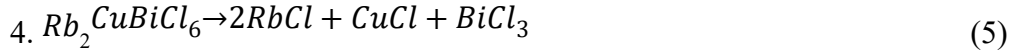
$$\Delta H_D = E(\text{K}_2\text{CuSbCl}_6) - 2E(\text{KCl}) - E(\text{CuCl}) - E(\text{SbCl}_3)$$



$$\Delta H_D = E(\text{Rb}_2\text{CuSbCl}_6) - 2E(\text{RbCl}) - E(\text{CuCl}) - E(\text{SbCl}_3)$$



$$\Delta H_D = E(K_2CuSbCl_6) - 2E(KCl) - E(CuCl) - E(BiCl_3)$$



$$\Delta H_D = E(K_2CuSbCl_6) - 2E(KCl) - E(CuCl) - E(BiCl_3)$$

Here  $E(A_2CuMCl_6)$ ,  $E(ACl_3)$ ,  $E(CuCl)$  and  $E(MCl_3)$  are respectively the total DFT energies of  $A_2CuMCl_6$ ,  $ACl_3$ ,  $CuCl$  and  $MCl_3$  and  $\Delta H_D$  is the decomposition energy.

Gibbs free energy fluctuations with respect to temperature have been graphically represented to affirm the thermodynamic stability of the provided materials.

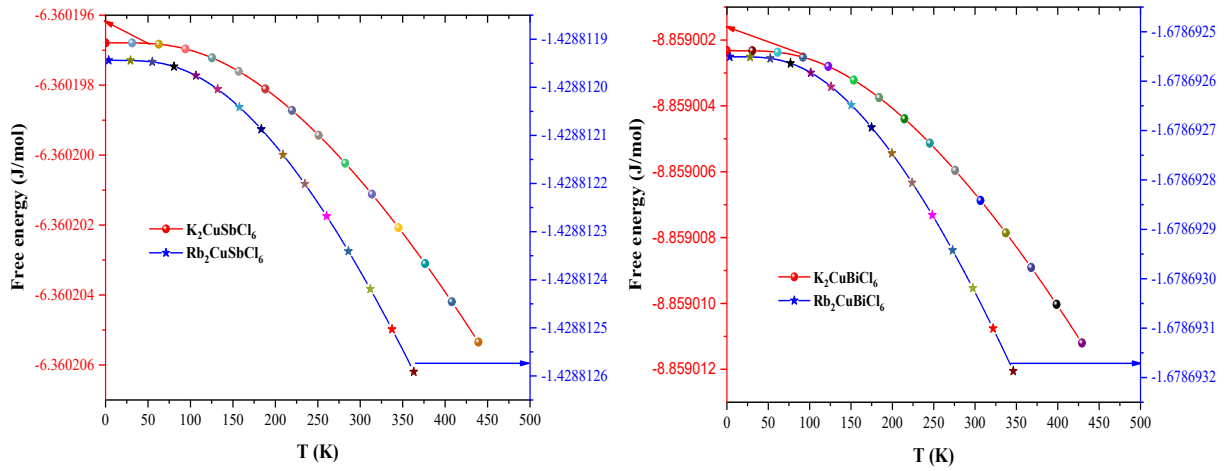


**Figure S2;** Gibbs free energy as a function of temperature of  $A_2CuMCl_6$  halide perovskites

The Gibbs free energy plots for the  $A_2CuMCl_6$  compounds, as shown in Figure S2 (a, b), demonstrate noticeable changes in vibrational free energy with increasing temperature across the given structures. Notably, a greater disparity in vibrational free energy corresponds to a heightened preference for a particular structure.

#### IV. Thermodynamic parameters: Specific heat ( $C_v$ ), Debye temperature ( $\theta_D$ ) and Gruisen parameter ( $\gamma$ )

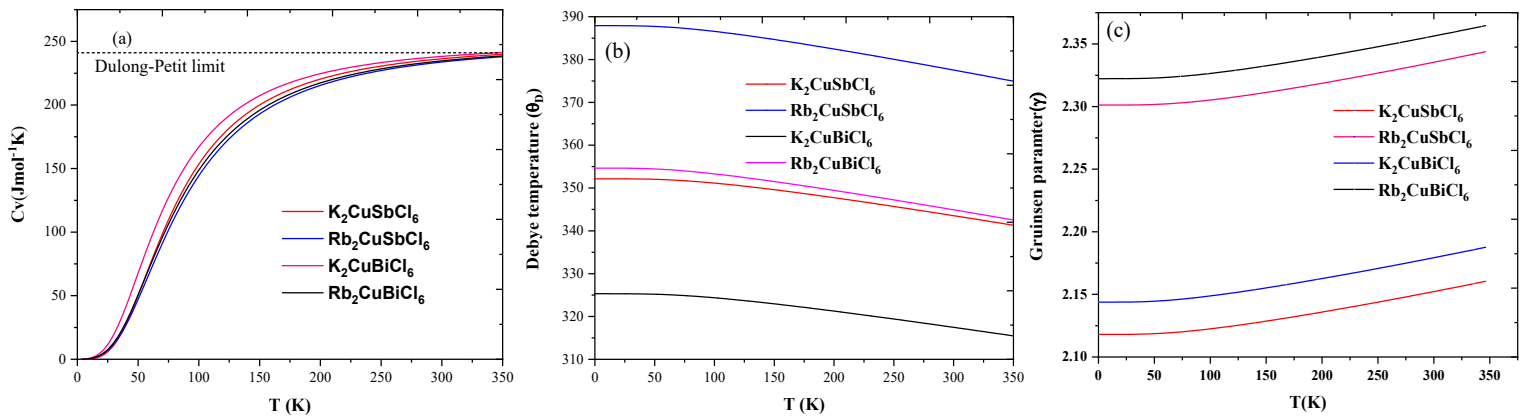


**Figure S3;** Plot of thermodynamic parameters (a) Specific heat, (b) Debye temperature and (d) Gruneisen parameter against temperature

The graphical interpretations of Specific heat, Debye temperature and Gruneisen parameter are shown in Figure S3(a-c). Specific heat, denoted as  $C_v$ , characterizes the amount of energy required to increase the temperature of a material by one degree. In this context,  $C_v$  can be understood as the energy storage capacity of the material corresponding to a specific temperature difference. If the material's temperature is subsequently reduced back to its initial level, the stored energy within  $C_v$  is released. Consequently, a higher heat capacity signifies a greater potential for energy storage, often indicative of the material's efficiency as a regenerator. The specific heat plot depicted in Figure S3 (a) illustrates how  $C_v$  changes concerning temperature variations for the mentioned materials. At lower temperatures,  $C_v$  adheres to a  $T^3$  law, signifying that exclusively longwave phonons are stimulated within this range. Notably, as the temperature rises, all phonons become thermally excited, leading  $C_v$  to converge towards the Dulong limit value of  $3nR$  ( $220 \text{ Jmol}^{-1}\text{K}$ ), where  $R$  symbolizes the gas constant.

The Debye temperature ( $\theta_D$ ) holds considerable significance as a thermoelastic characteristic of solids. It signifies the upper limit of temperature within which the constituents exhibit interlinked vibrations, reaching their peak modes of vibration. Figure S3(b) visually demonstrates that  $\theta_D$  exhibits a decline as temperature ascends. When temperatures are low, both thermal expansion and anharmonicity have limited effects, resulting in a near-constant Debye temperature. During this low-temperature regime, the high-frequency vibration modes become constrained, leaving only the acoustic modes to be activated. As temperature rises, the Debye temperature ( $\theta_D$ ) diminishes, leading to observable changes in the vibration spectra of the particles. Specifically, the increment in temperature prompts a reduction in  $\theta_D$ , allowing a broader range of vibration modes to become active. Notably, the estimated Debye temperature values for  $\text{K}_2\text{CuSbCl}_6$ ,  $\text{Rb}_2\text{CuSbCl}_6$  and  $\text{K}_2\text{CuBiCl}_6$ ,  $\text{Rb}_2\text{CuBiCl}_6$  at 0 GPa are 352 K, 387 K, 325 K, 355 K, respectively.

The Gruneisen parameter ( $\gamma$ ) is used to measure the anharmonicity in the crystals. Fig. S3(c) represents the variations in  $\gamma$  with temperature, advocates rise in anharmonicity increases with the temperature, although the variation is sluggish. The atomic vibrations increase vigorously with temperature due to which  $\gamma$ -parameter also increases.

## **V. Calculations of mechanical stability parameters of $\text{A}_2\text{CuMCl}_6$ double halide perovskites**

In Voigt -Reuss-Hill method, Bulk and Shear moduli are presented as:

$B_V = \frac{(C_{11} + 2C_{12})}{3}$  and  $G_V = \frac{(C_{11} + C_{12} + 3C_{44})}{5}$ , where  $B_V$  and  $G_V$  are Voigt and Reuss bounds. The Bulk and Shear moduli in Reuss approximations are framed as below.

$$B_V = B_R \quad \text{and} \quad G_R = \frac{5(C_{11} - C_{12})C_{44}}{4C_{44} + 3(C_{11} - C_{12})}$$

In the Hill approximation, the bulk and shear moduli are computed by taking the arithmetic mean of  $B_V$ ,  $B_R$ , and  $G_V$ ,  $G_R$ , respectively, as expressed by the following formulae.

$$B = \frac{(B_V + B_R)}{2} \quad \text{and} \quad G = \frac{(G_V + G_R)}{2}$$

The Young's modulus and Poisson's ratio are determined from the bulk and shear moduli using the relations given as:

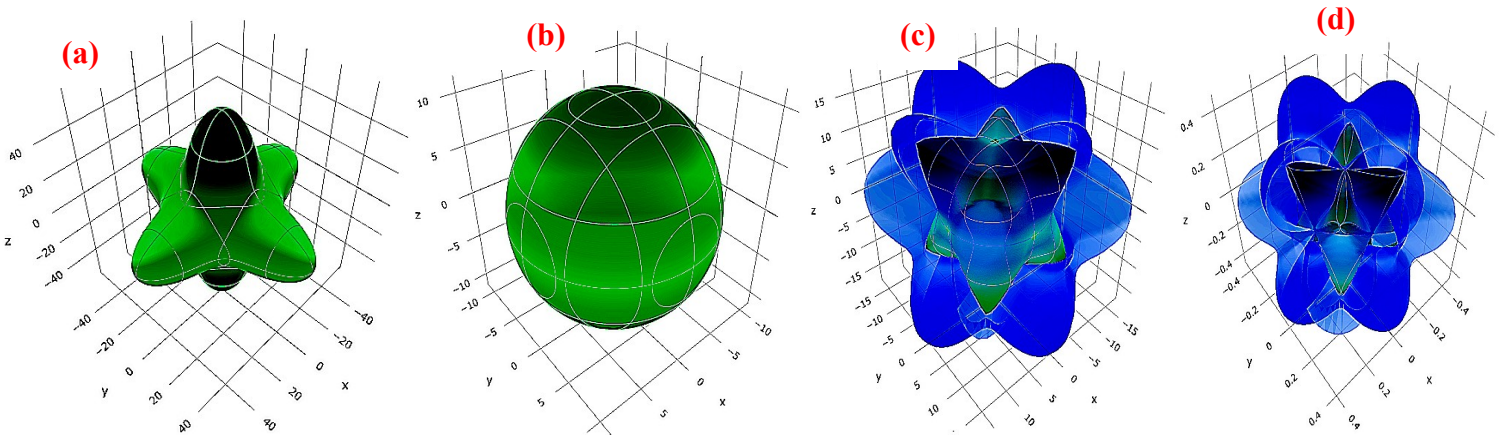
$$Y = \frac{9BG}{3GB + B} \quad \text{and} \quad \nu = \frac{3B - Y}{6B}$$

Lame's coefficients and Kleiman parameter are given by the following equations:

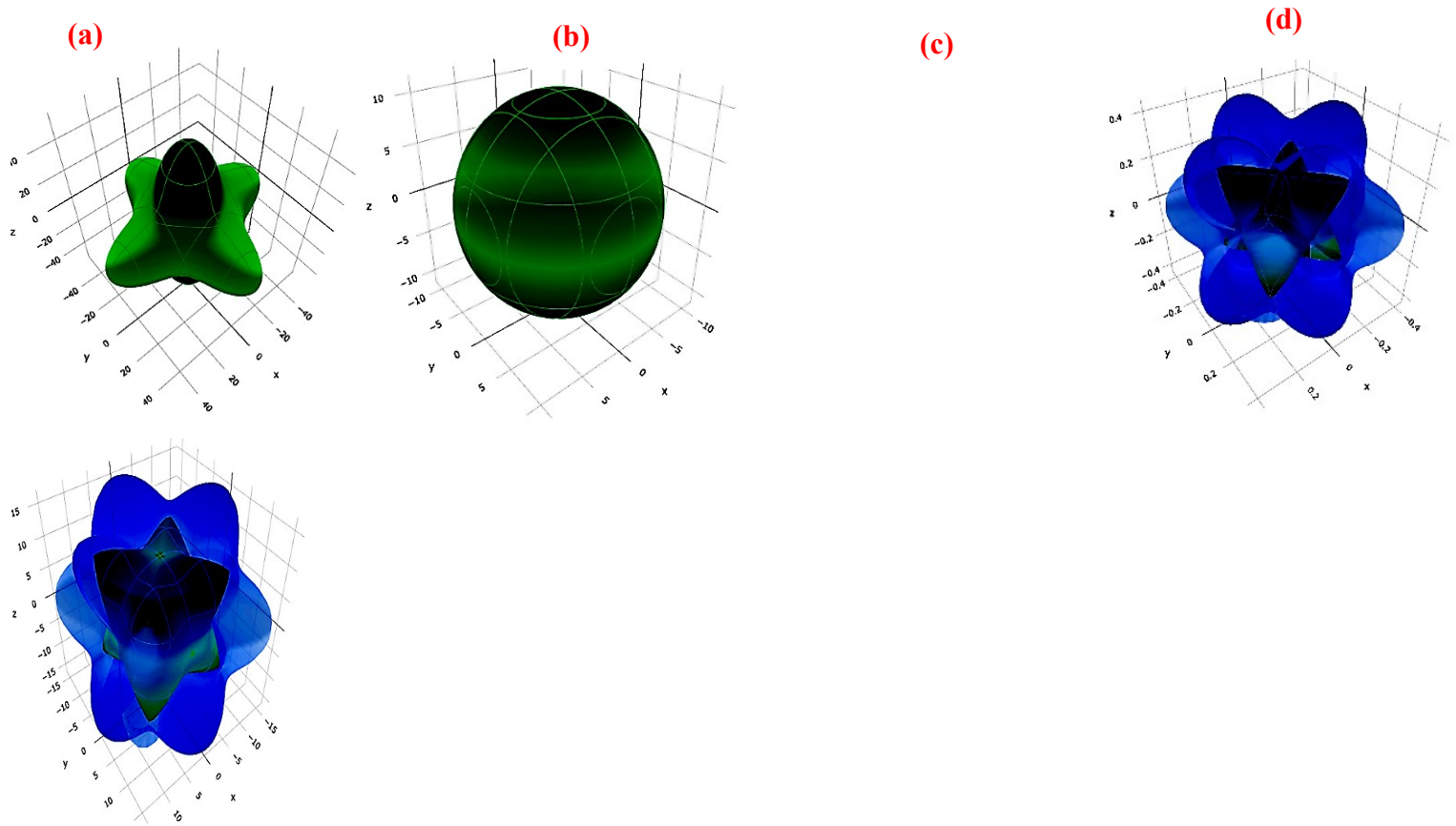
$$\lambda = \frac{\nu Y}{(1 + \nu)(1 + 2\nu)}, \quad \beta = \frac{E}{2(1 + \nu)} \quad \text{and} \quad \zeta = \frac{C_{11} + 8C_{12}}{7C_{11} + 2C_{12}}$$

## VI. Three-dimensional graphics of Young's modulus, (b) linear compressibility, (c) Shear modulus, and (d) Poisson's ratio of $A_2CuMCl_6$ perovskites

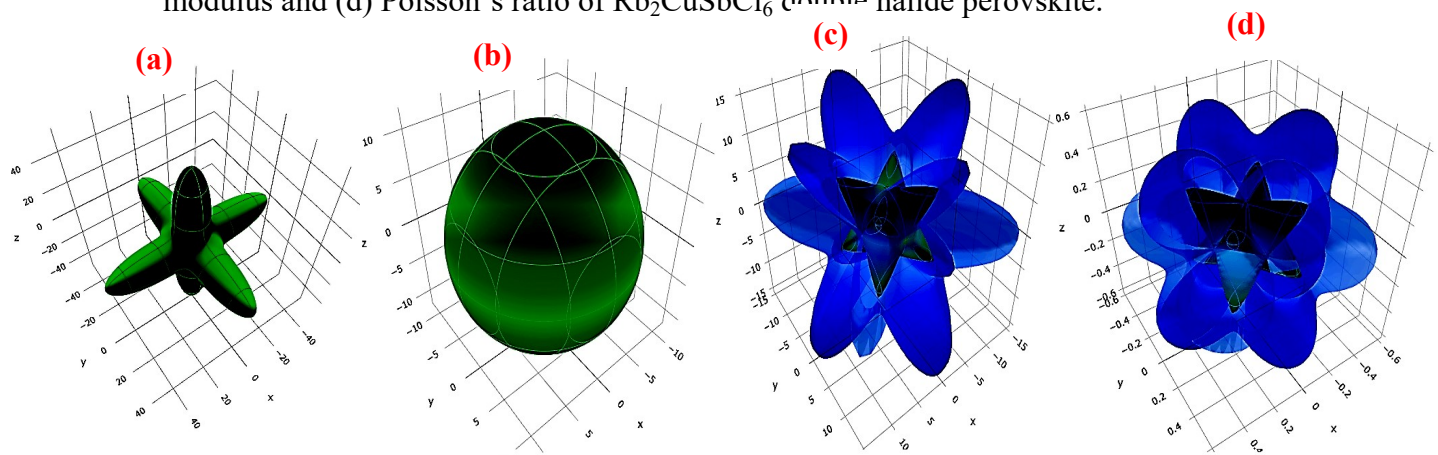
The three-dimensional graphical representations of (a) Young's modulus, (b) linear compressibility, (c) Shear modulus, and (d) Poisson's ratio for the provided materials are displayed below.



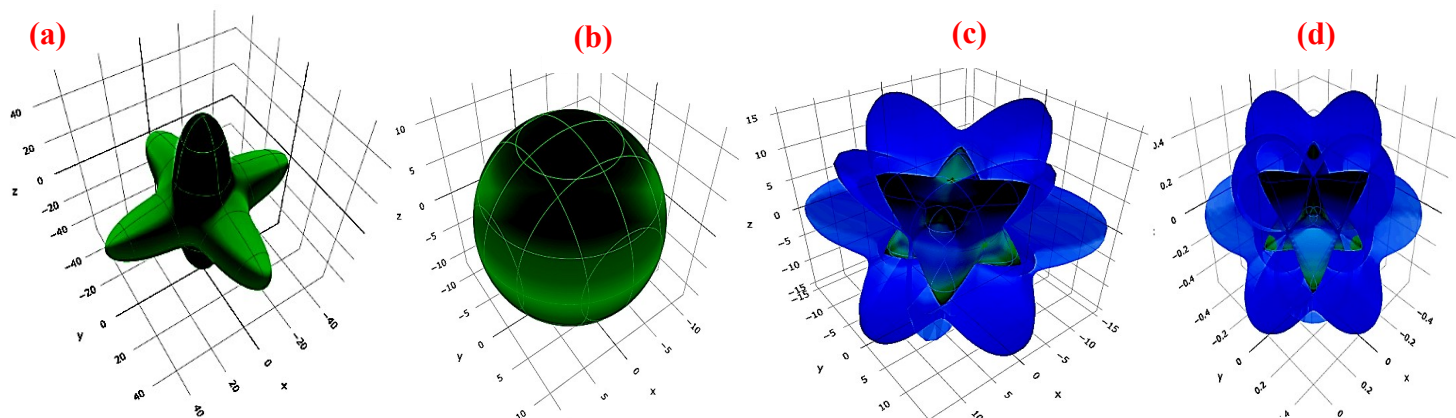
**Figure S4;** Three-dimensional graphical interpretations of Young's modulus, (b) linear compressibility, (c) Shear modulus and (d) Poisson's ratio of  $K_2CuSbCl_6$  double halide perovskite.



**Figure S5:** Angular dependency of Young's modulus, (b) linear compressibility, (c) Shear modulus and (d) Poisson's ratio of  $\text{Rb}_2\text{CuSbCl}_6$  double halide perovskite.

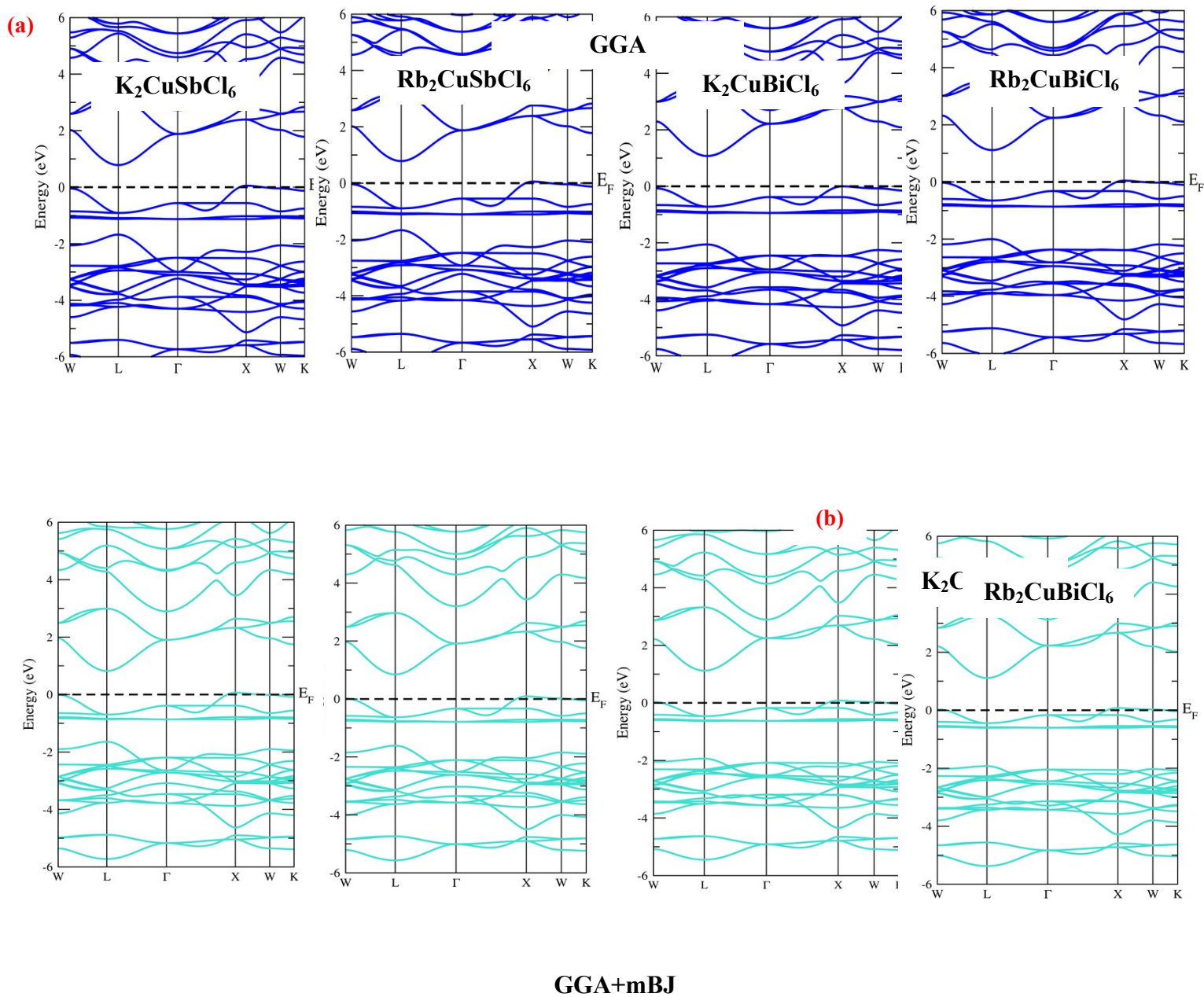


**Figure S6:** Three-dimensional graphical representations of Young's modulus, (b) linear compressibility, (c) Shear modulus and (d) Poisson's ratio of  $\text{K}_2\text{CuBiCl}_6$  double halide perovskite.



**Figure S7:** Spatial dependence of Young's modulus, (b) linear compressibility, (c) Shear modulus and (d) Poisson's ratio of  $\text{Rb}_2\text{CuBiCl}_6$  double halide perovskite

### VII. Calculation of Electronic band structure using different exchange correlational functionals.



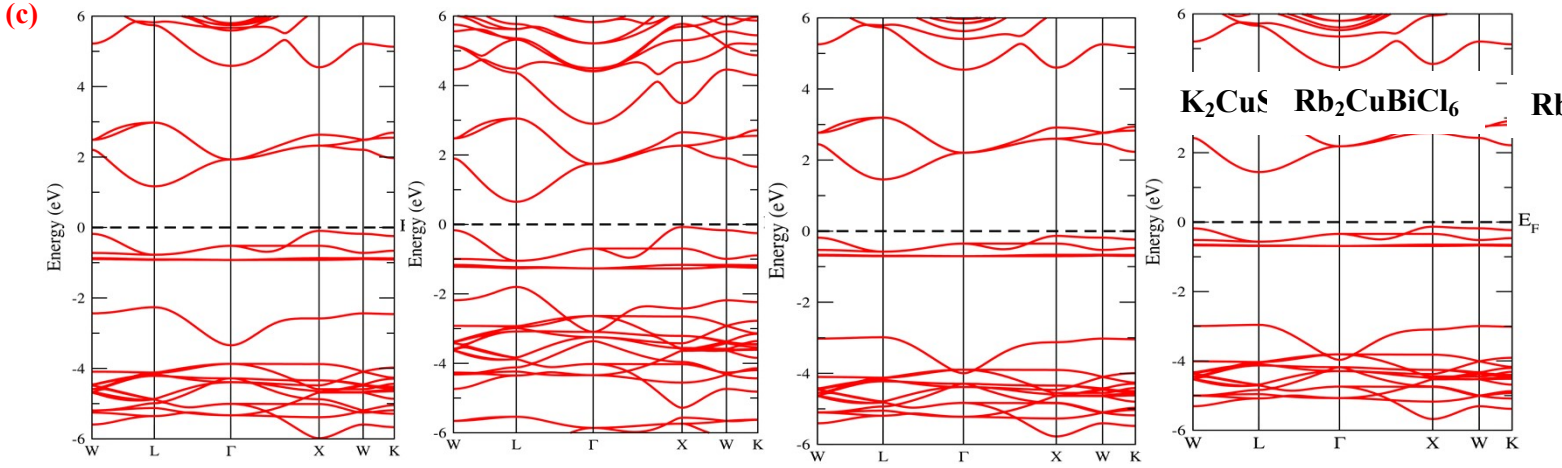


**Figure S8;** Electronic band structure of  $A_2CuMCl_6$  double halide perovskites determined *via* (a) GGA-PBE functional, (b) GGA+U functional, (c) GGA+mBJ functional.

### VIII. Thermal conductivity ( $\kappa$ ) of $A_2CuMCl_6$ (A=K, Rb M=Sb, Bi) double perovskites

The electronic thermal conductivity has been computed using BoltzTraP code as discussed in above section. However, the lattice thermal conductivity has been computed using Slack's model

which is given as [3]; 
$$\kappa_l = \frac{A\theta_D^3 V^{1/3} m}{\gamma^2 N^{2/3} T},$$
 where the symbols assume their usual meanings. The Slack model emphasizes that the Debye temperature ( $\theta_D$ ), Gruneisen parameter ( $\gamma$ ), temperature (T), volume (V), average molar mass per atom (m), and the number of atoms per unit cell (N) all impact the lattice thermal conductivity. The parameter A is determined as; [3]

$$A = \frac{2.43 \times 10^8}{1 - \frac{0.514}{\gamma} + \frac{0.228}{\gamma^2}}.$$

Utilizing these associated factors, the Slack model has been implemented to calibrate the lattice thermal conductivity.

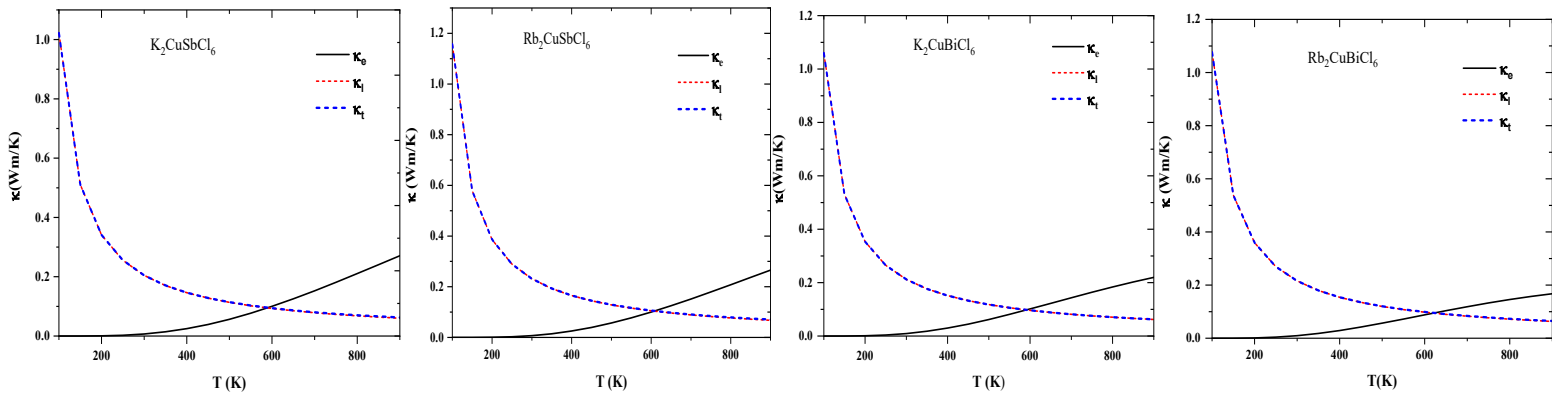
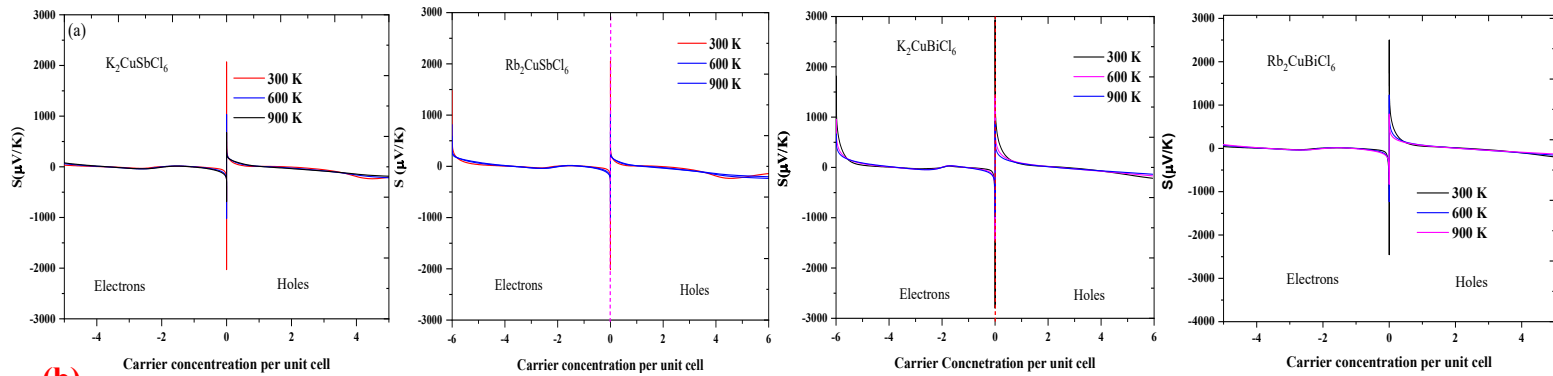


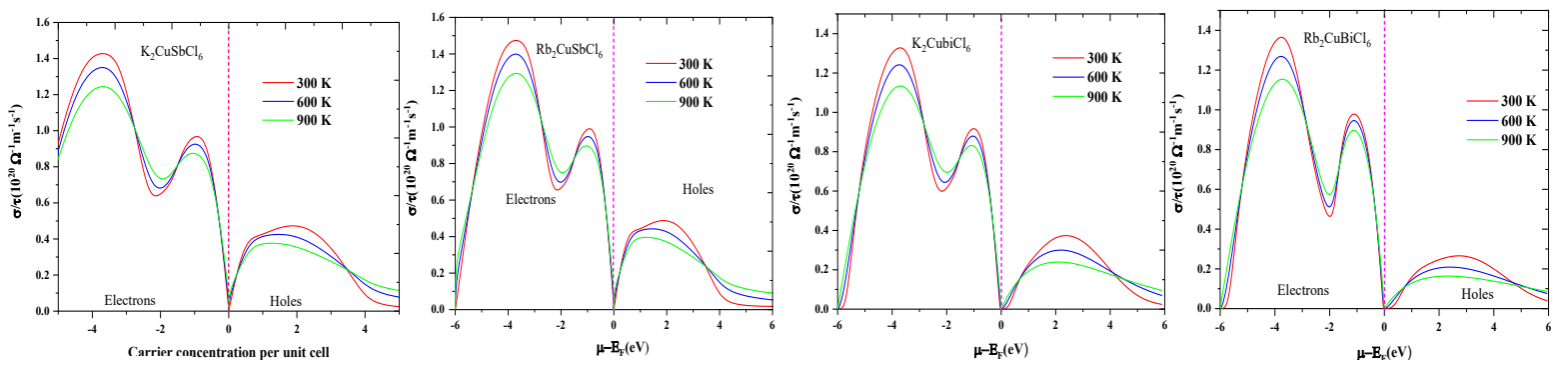
**Figure S9;** Calculated (a) electronic thermal conductivity, (b) lattice thermal conductivity and (c) total thermal conductivity in  $A_2CuMCl_6$  double perovskites.

## IX. Variation of Seebeck coefficient, electrical conductivity, and figure of merit against carrier concentration.

(a)



(b)



(c)

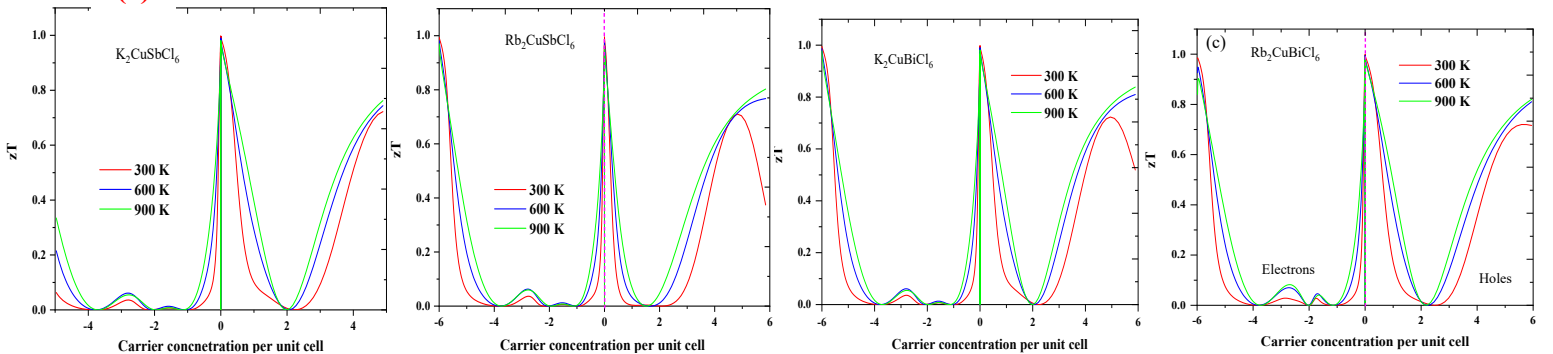


**Figure S10.** Thermoelectric parameters of  $\text{A}_2\text{CuMCl}_6$  (a) Seebeck coefficient, (b) electrical conductivity and (c) figure of merit ( $zT$ ) against carrier concentration at different temperatures (300 K, 600 K, 900 K)

## X. Computed optical properties of $\text{A}_2\text{CuMCl}_6$ double halide perovskites.

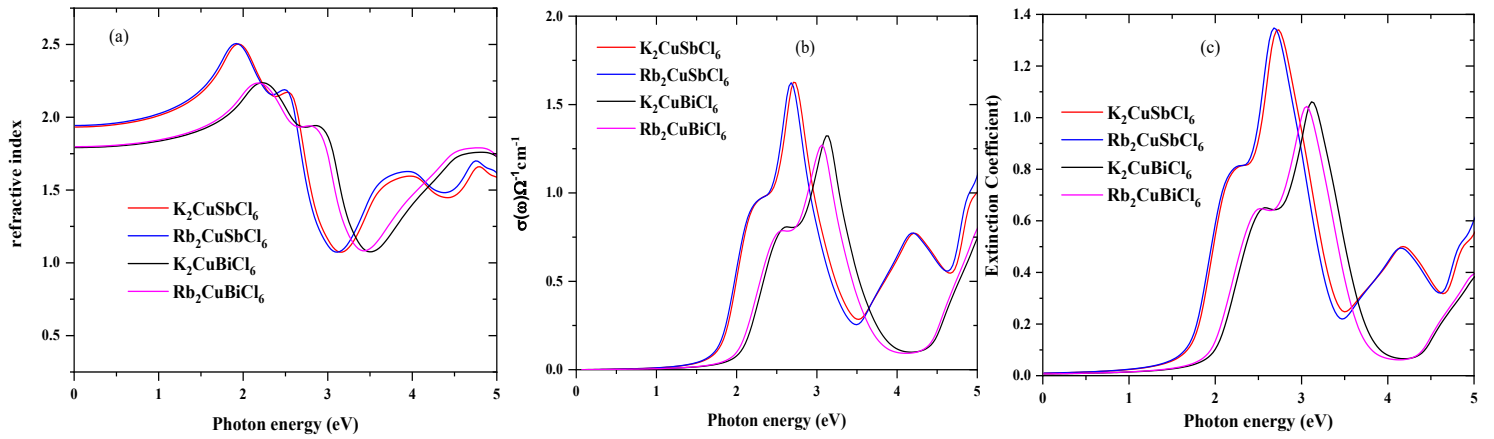


**Figure S11;** Optical coefficients of  $A_2CuMCl_6$  halide perovskites (a) refractive index, (b) optical conductivity and (c) extinction coefficient against photon energy.

An important optical property that provides insights into the behaviour of light within a material is the refractive index. The variation of the refractive index with photon energy is depicted in Figure S11(a). The static refractive index values for  $K_2CuSbCl_6$ ,  $Rb_2CuSbCl_6$ ,  $K_2CuBiCl_6$  and  $Rb_2CuBiCl_6$  are 2.5, 2.55 and 2.05, 2.08 respectively. They reach a maximum value around 2 eV, reflecting the behaviour of the material in response to light absorption at different energies. The optical conductivity, denoted as  $\sigma(\omega)$ , provides insight into the available charge carriers for conduction. Its pattern closely mirrors that of the absorption spectra, depicted in Figure S11(b). Across the entire range of photon energies (0–4 eV), the conductivity profile exhibits alternating high and low peaks, accompanied by the presence of a distinctive hump at specific energy levels. Notably, the maximum conductivity is observed within the higher energy range.

The extinction coefficient essentially constitutes the complex portion of the refractive index, illustrating the way electromagnetic waves propagate through a given medium. As depicted in Figure S11 (c), the extinction coefficient exhibits a division into three prominent absorption peaks, each centered within a distinct range of photon energies. These diverse peaks emerge because of electronic transitions between different energy levels.

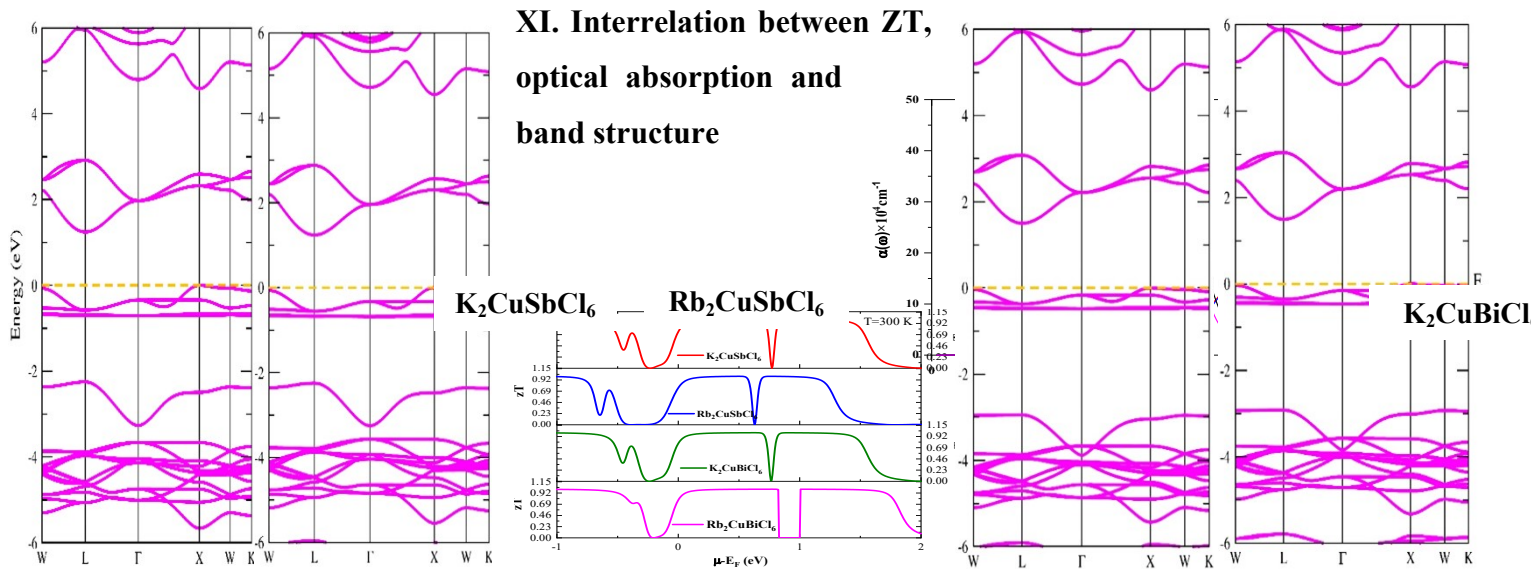


**Figure S12.** Variation in the ZT and absorption coefficient of  $A_2CuMCl_6$  halide perovskites altogether with the band profile.

## XII. Calculation of Phonon dynamics

We utilized Density Functional Perturbation Theory (DFPT) as implemented in the Quantum Espresso Code to compute the phonon spectrum across various wave vectors. The dynamical matrix is solved to calculate phonon frequencies and displacement patterns, dielectric tensors, effective charges.

The electron-phonon coefficients  $g$  are defined as

$$g_{\mathbf{q}\nu}(\mathbf{k}, i, j) = \left( \frac{\hbar}{2M\omega_{\mathbf{q}\nu}} \right)^{1/2} \langle \psi_{i,\mathbf{k}} | \frac{dV_{SCF}}{d\hat{u}_{\mathbf{q}\nu}} \cdot \hat{\epsilon}_{\mathbf{q}\nu} | \psi_{j,\mathbf{k}+\mathbf{q}} \rangle$$

The phonon linewidth  $\gamma_{\mathbf{q}\nu}$  is defined by:

$$\gamma_{\mathbf{q}\nu} = 2\pi\omega_{\mathbf{q}\nu} \sum_{ij} \int \frac{d^3k}{\Omega_{BZ}} |g_{\mathbf{q}\nu}(\mathbf{k}, i, j)|^2 \delta(e_{\mathbf{q},i} - e_F) \delta(e_{\mathbf{k}+\mathbf{q},j} - e_F)$$

while the electron-phonon coupling constant  $\lambda_{\mathbf{q}\nu}$  for mode  $\nu$  at wavevector  $\mathbf{q}$  is defined as

$$\lambda_{\mathbf{q}\nu} = \frac{\gamma_{\mathbf{q}\nu}}{\pi \hbar N(e_F) \omega_{\mathbf{q}\nu}^2}$$

where  $N(e_F)$  is the DOS at the Fermi level. The spectral function is defined as:

$$\alpha^2 F(\omega) = \frac{1}{2\pi N E_F} \sum_{q\nu} \delta(\omega - \omega_{q\nu}) \frac{\gamma_{q\nu}}{\hbar \omega_{q\nu}}$$

The electron-phonon mass enhancement parameter  $\lambda$  can also be defined as the first

$$\lambda = \sum_{q\nu} \lambda_{q\nu} = 2 \int \alpha^2 F(\omega)$$

reciprocal momentum of the spectral function:

Note that a factor  $M^{-1/2}$  is hidden in the definition of normal modes as used in the code. McMillan:

$$T_c = \frac{\Theta_D}{1.45} \exp \left[ \frac{-1.04(1 + \lambda)}{\lambda(1 - 0.62\mu^*) - \mu^*} \right]$$

or (better?)

$$T_c = \frac{\omega_{log}}{1.2} \exp \left[ \frac{-1.04(1 + \lambda)}{\lambda(1 - 0.62\mu^*) - \mu^*} \right]$$

Where,

$$\omega_{log} = \exp \left[ \frac{2}{\lambda} \int \frac{d\omega}{\omega} \alpha^2 F(\omega) \log \omega \right]$$

## XIII. $k$ -point convergence in $A_2CuMCl_6$ double halide perovskites

To ensure the accuracy of our calculations, we conducted a comprehensive analysis of property convergence, encompassing key parameters such as energy (E), Seebeck coefficient (S), and both the imaginary (Im( $\epsilon$ )) and real (Re( $\epsilon$ )) parts of the dielectric function. This investigation was carried out specifically for the present halide perovskites and their dependence on  $k$ -points. The results, as presented in Table S2 for the  $A_2CuMCl_6$ , confirm that utilizing 1000  $k$ -points provides sufficient accuracy for calculating energy (E).

**Table S2:** Energies (eV) of  $A_2CuMCl_6$  (A=K, Rb M=Sb, Bi) double perovskites at different  $k$ -points calculated using PBE  $\epsilon_{xc}$  functional.

Configuration	500	1000	1500	2000
$K_2CuSbCl_6$	-329456.231	-329456.233	-329456.235	-329456.237
$Rb_2CuSbCl_6$	-458893.511	-458893.512	-458893.515	-458893.518
$K_2CuBiCl_6$	-740119.970	-740119.971	-740119.973	-740119.974
$Rb_2CuBiCl_6$	-869557.274	-869557.276	-869557.277	-869557.278

**Table S3:** Seebeck coefficient ( $\mu V/K$ ) of  $A_2CuMCl_6$  (A=K, Rb M=Sb, Bi) double halide perovskites at different  $k$ -points calculated using HSE06  $\epsilon_{xc}$  functional. It's important to note that thermoelectric parameters are highly sensitive to  $k$ -point sampling. Therefore, we utilized a higher  $k$ -mesh for these calculations, and it was established that 100,000- $k$  points proved to be adequate for accurately computing the thermoelectric coefficients.

Configuration	50000	100000
$K_2CuSbCl_6$	2095.01	2100.03
$Rb_2CuSbCl_6$	1997.83	2000.10
$K_2CuBiCl_6$	2894.74	2899.95
$Rb_2CuBiCl_6$	2587.52	2600.51

**Table S4:** The maximum values of the real and imaginary parts of the dielectric constants for  $A_2CuMCl_6$  (A=K, Rb; M=Sb, Bi) double halide perovskites were calculated (within the energy range of (0-4) eV using the HSE06  $\epsilon_{xc}$  functional. Typically, a higher  $k$ -mesh than usual is needed to accurately compute optical parameters. It has been determined that employing a 5000- $k$  point mesh is sufficient for calculating the optical coefficients.

Configuration	2000		4000		5000	
	$\epsilon_1(\omega)$	$i\epsilon_1(\omega)$	$\epsilon_1(\omega)$	$i\epsilon_1(\omega)$	$\epsilon_1(\omega)$	$i\epsilon_1(\omega)$

<b>K<sub>2</sub>CuSbCl<sub>6</sub></b>	5.93	4.88	5.93	4.91	5.94	4.91
<b>Rb<sub>2</sub>CuSbCl<sub>6</sub></b>	6.00	5.02	6.02	5.00	6.02	5.00
<b>K<sub>2</sub>CuBiCl<sub>6</sub></b>	4.96	3.44	4.95	3.45	4.95	3.45
<b>Rb<sub>2</sub>CuBiCl<sub>6</sub></b>	5.00	3.55	5.01	3.54	5.01	3.54

## References:

1. Zhou, W. et al. Lead-free small-bandgap Cs<sub>2</sub>CuSbCl<sub>6</sub> double perovskite nanocrystals. *J. Phys. Chem. Lett.* 11, 6463–6467 (2020).
2. Eric T. McClure, Molly R. Ball, Wolfgang Windl, and Patrick M Woodward. Cs<sub>2</sub>AgBiX<sub>6</sub> (X = Br, Cl) — New visible light absorbing, lead-free halide perovskite semiconductors. *Chem. of Mat.* DOI: 10.1021/acs.chemmater.5b0423.
3. Nath, P. et al. High throughput combinatorial method for fast and robust prediction of lattice thermal conductivity. *Scr. Mater.* 129, 88–93 (2017).
4. Photovoltaic absorbers based on first-principles spectroscopic screening of materials. *Phys. Rev. Lett.* 2012, 108 (6), 068701.